CAMBRIDGE
UNIVERSITY PRESS

Article

Theoretical analysis of the effect of doping with Na(I), K(I), Mg(II), Ca(II) and Fe(II) on the electronic and mechanical properties of pyrophyllite

Jian Zhao[1,2], Yi-Fei Wang[1,2] (ID), Zhao-Long Luan[1,2], Yu Cao[1,2] and Man-Chao He[1]

[1]State Key Laboratory of Geomechanics and Deep Underground Engineering, China University of Mining and Technology, Beijing, China and [2]School of Mechanics and Civil Engineering, China University of Mining and Technology, Beijing, China

Abstract

Pyrophyllite is an important layered phyllosilicate material that is used in many fields due to its beneficial physicochemical and mechanical properties. Due to the presence of multiple defects in pyrophyllite, an in-depth investigation was conducted using density functional theory to explore the effects of Na(I), K(I), Mg(II), Ca(II) and Fe(II) doping on the atomic structure, electronic properties and mechanical characteristics of pyrophyllite. The results demonstrated that, among the studied defects, K(I) doping had the most pronounced effects on the lattice constants and bonding lengths of pyrophyllite, while the least significant effects were observed in the case of Fe(II) doping. Moreover, the partial and total densities of states and band structures of the five kinds of doped pyrophyllite also changed significantly due to the redistribution of electrons. Finally, the elastic constants of the doped pyrophyllite were lower than that of the undoped pyrophyllite. Doping with Na(I), K(I), Mg(II), Ca(II) and Fe(II) reduced the deformation resistance, stiffness and elastic wave velocity but increased the degree of anisotropy in pyrophyllite. The observed effects on the mechanical properties of pyrophyllite followed the order: Mg(II) > Fe(II) > Ca(II) > K(I) > Na(I).

As a crucial type of layered material, phyllosilicate minerals have played a significant role in human life and civilization for a long time (Zhang *et al.*, 2014). Pyrophyllite is one of the most abundant phyllosilicate minerals (Du & Yuan, 2019). Because of its beneficial physicochemical and mechanical properties (Zhao *et al.*, 2021a), pyrophyllite is used in construction materials, ceramics, refractories, chemicals, the paper and coating industries and other fields (Bentayeb *et al.*, 2003). Therefore, many researchers have investigated the physicochemical and mechanical properties of pyrophyllite using experimental and theoretical computation methods (Refson *et al.*, 2003; Katti *et al.*, 2005; Shi *et al.*, 2017), increasing our understanding of pyrophyllite, which is now considered viable for use in coatings, medicines, cosmetics, the aerospace industry and other fields (Ali *et al.*, 2021; Luna *et al.*, 2021).

However, natural pyrophyllite includes a wide range of defect elements. Yan *et al.* (2013) measured the mass fractions of Na_2O, MgO, K_2O and Fe_2O_3 in pyrophyllite samples from Zhejiang Province, China, and found them to be 0.27, 0.13, 0.67 and 0.45 wt.%, respectively. Reddy *et al.* (2016) determined the mass fractions of Na_2O, MgO, K_2O, Fe_2O_3 and CaO in pyrophyllite minerals from California at 0.10, 0.01, 0.20, 0.20 and 0.09 wt.%, respectively. Based on above results and other data (Yan *et al.*,

2013; Reddy *et al.*, 2016; Shi *et al.*, 2017), the primary contaminant defect elements in pyrophyllite are Na(I), K(I), Mg(II), Ca(II) and Fe(II), with concentration ranges of 0.04–0.27, 0.02–0.35, 0.01–0.47, 0.02–0.31 and 0.07–0.54 wt.%, respectively.

As is well known, metal cations often enter pyrophyllite crystals *via* cation substitution (Zhao, 2013). The differences in the sizes and charges of the ions that substituted into pyrophyllite affect the atomic and electronic structures of pyrophyllite, leading to changes in the physicochemical and mechanical properties of pyrophyllite (Zhao, 2013). Ali *et al.* (2021) experimented with minor iron doping into pyrophyllite, which resulted in a reduction in the melting point of refractories, influenced the transparency of glass products and decreased the transmission capabilities of optical fibres. Luna *et al.* (2021) highlighted the impacts on the work function, magnetic moment and other parameters when doping pyrophyllite with Mg(II), Fe(II) and Fe(III). Based on the above experimental results, the primary contaminant defect elements of pyrophyllite are Na(I), K(I), Mg(II), Ca(II) and Fe(II). To the best of the authors' knowledge, the effects of doping using these five elements on the electronic structure and mechanical properties of pyrophyllite have not been established. Greater insights into the doping effects of Na(I), K(I), Mg(II), Ca(II) and Fe(II) on the various properties of pyrophyllite are needed, which could be obtained through detailed first-principles calculations at the molecular level.

In this work, the doping formation mechanism and influences of Na(I), K(I), Mg(II), Ca(II) and Fe(II) doping on the atomic and mechanical characteristics of pyrophyllite were calculated

Cite this article: Zhao J, Wang Y-F, Luan Z-L, Cao Y, He M-C (2023). Theoretical analysis of the effect of doping with Na(I), K(I), Mg(II), Ca(II) and Fe(II) on the electronic and mechanical properties of pyrophyllite. *Clay Minerals* **58**, 113–120. https://doi.org/10.1180/clm.2023.17

using density functional theory (DFT). By comparing the lattice parameters, the partial density of state (PDOS), total density of state (TDOS), the band structure and the elastic constants of pyrophyllite with various doping agents, the effects of doping on these physicochemical and mechanical properties can be obtained. The objective of this study was to use a first-principles approach to obtain an understanding of the various properties associated with various point defects in pyrophyllite at the molecular level.

Materials and methods

The *Vienna Ab initio Simulation Package* (*VASP*; Kresse & Furthmüller, 1996; Tunega *et al.*, 2012) was applied to pyrophyllite with the molecular formula $Al_4Si_8O_{24}H_4$ and space group *P*1. The calculation of the exchange correlation energy was performed using the Perdew–Burke–Ernzerhof (PBE) density functional (Perdew *et al.*, 1996; Putra *et al.*, 2019). Through the utilization of calculated Hellmann–Feynman forces, a comprehensive relaxation of all atomic positions in pyrophyllite was performed. The energy cutoff for the plane-wave basis was 600 eV. To optimize the atomic geometries, a conjugate-gradient algorithm was employed, refining the positions of the atoms iteratively. The optimization process continued until the residual force acting on the atoms reached a threshold of <0.01 eV $Å^{-1}$ (Zhao *et al.*, 2020). The $9 \times 5 \times 5$ Monkhorst–Pack (Chen *et al.*, 2020; Hou *et al.*, 2020; Zhao *et al.*, 2021a) *k*-points set was used. The valence electrons of pyrophyllite included $1s^1$ of H, $2s^2$ and $2p^4$ of O, $3s^2$ and $3p^1$ of Al and $3s^2$ and $3p^2$ of Si. The valence electrons of doped atoms in the pyrophyllite included $3p^63d^64s^2$ of Fe, $2p^63s^2$ of Mg, $2p^63s^1$ of Na, $2p^63s^23p^64s^1$ of K and $2p^63s^23p^64s^2$ of Ca.

All of the calculations were performed using a $1 \times 1 \times 1$ unit cell (containing 40 atoms) as shown in Fig. 1. The defect system was modelled by arranging for a defect to substitute for Al atoms of a periodic unit cell (Fig. 1a). The $1 \times 1 \times 1$ unit cell was chosen to provide sufficient lattice sites to accommodate defect concentrations as low as 0.037–0.149 wt.%, similar to previous studies. First, the doping mechanism of various metal defect substitutions of the pyrophyllite Al ion was calculated (Fig. 1a). To determine the doping mechanism of various metal defects in the pyrophyllite, the formation energy $E_f(X, q)$ was calculated, given by Equation 1 (Walle & Neugebauer, 2004):

$$E_f = E_{tot}(X, q) - E_{(pyrophyllite)} + n_i u_i - n_X u_X + q[E_F + E_V + \Delta V]$$ (1)

where $E_{tot}(X,q)$ and $E_{(pyrophyllite)}$ are the energies of the doped and defect-free pyrophyllite systems, respectively; n_i and n_X are the

Table 1. Total energy of the pyrophyllite system with various types of dopant atom and the formation energies of the dopant atoms.

Pyrophyllite	Number of dopant atoms	Total energy, $E_{tot}(X,q)$ (eV)	Formation energy of dopant atoms (eV)
Undoped	0	−294.710	–
Na-doped	1	−286.728	4.886
K-doped	1	−286.827	5.229
Mg-doped	1	−289.023	3.492
Ca-doped	1	−289.165	3.810
Fe-doped	1	−293.507	1.165

numbers of Al (Si, H or O) and Na (K, Mg, Ca or Fe) atoms of the unit cell, respectively; and u_i and u_X represent the chemical potentials of Al (Si, H or O) and Na (K, Mg, Ca or Fe) atoms, respectively. E_F represents the Fermi energy measured from the valence band maximum E_V of the undoped pyrophyllite, and ΔV is a correction term for aligning the electrostatic potential to E_V.

Table 1 presents the formation energy results of five kinds of defects in the pyrophyllite. The formation energies of the Na(I), K(I), Mg(II), Ca(II) and Fe(II) doping were 4.886, 5.229, 3.492, 3.810 and 1.165 eV, respectively, denoting that heat needed to be absorbed from outside during doping. The formation energy of Fe(II)-doped pyrophyllite was the lowest, with the other formation energies following the order of Mg(II) < Ca(II) < Na(I) < K(I). These results indicate that the stability of the Fe(II)-doped pyrophyllite was greater than those of the other doped pyrophyllites, and the Fe atoms were substituted for the Al atoms of the pyrophyllite more easily than the other doping ions.

Based on the above optimized structure of the pyrophyllite with metal doping, other properties were investigated further. By subjecting the equilibrium lattice to stress tensors with small strains, the elastic constants C_{ij} of the crystalline systems were determined based on the corresponding changes in the total energy of the unit cell. In this work, the strain amplitude δ was varied with steps of 0.01 from –0.06 to 0.06 (Qin *et al.*, 2020). The bulk modulus (*B*; Equation 2) and shear modulus (*G*; Equation 3) of pyrophyllite can be calculated using the Voigt–Reuss–Hill (VRH) approximation based on the elastic constants obtained (Hill, 1952; Chung & Buessem, 1968):

$$B = \frac{B_V + B_R}{2}$$ (2)
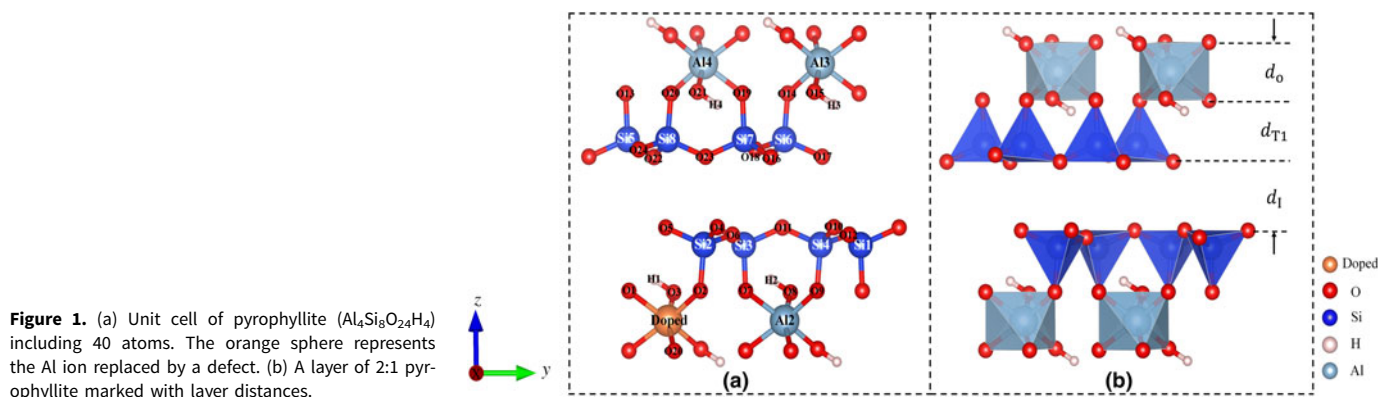
$$G = \frac{G_V + G_R}{2}$$ (3)

Figure 1. (a) Unit cell of pyrophyllite ($Al_4Si_8O_{24}H_4$) including 40 atoms. The orange sphere represents the Al ion replaced by a defect. (b) A layer of 2:1 pyrophyllite marked with layer distances.

For a detailed computation of B_R, B_V, G_R and G_V, see Qin *et al.* (2020). Young's modulus (Y), Poisson's ratio (μ), acoustic compression (v_p) wave velocity and shear (v_s) wave velocity were obtained using Equations 4–7.

$$Y = \frac{9BG}{3B + G} \quad (4)$$

$$\mu = \frac{3B - 2G}{2(3B + G)} \quad (5)$$

$$v_p = \sqrt{\frac{3B + 4G}{3\rho}} \quad (6)$$

$$v_s = \sqrt{\frac{G}{\rho}} \quad (7)$$

where ρ represents the density of the pyrophyllite.

Results and discussion

Effects on the atomic structure of pyrophyllite

Pyrophyllite, with the ideal structural formula $Al_4Si_8O_{24}H_4$, is a planar 2:1 phyllosilicate composed of two-dimensional mineral layers. Existing experimental data (Gruner, 1934; Lee & Guggenheim, 1981) and previously calculated results (Bruno *et al.*, 2006; Kremleva *et al.*, 2012; Lavikainen *et al.*, 2015) regarding the pyrophyllite layers provided the data basis for the establishment of the structure of pyrophyllite (Zhang *et al.*, 2010). In our first-principles calculations, an atomic structure was determined to represent the positions of atoms and lattice parameters after optimization. Table 2 shows the lattice parameters of undoped pyrophyllite and Na(I)-, K(I)-, Mg(II)-, Ca(II)- and Fe(II)-doped pyrophyllite. The calculated structural parameters of undoped pyrophyllite were consistent with previous experimental data (Gruner, 1934; Lee & Guggenheim, 1981). Compared to the lattice parameters of undoped pyrophyllite and doped pyrophyllite, as listed in Table 2, the effects of K(I) doping on pyrophyllite were the greatest, and the least effects were observed for Fe(II) doping of pyrophyllite.

Table 3 shows the average calculated bond lengths of the undoped and doped pyrophyllites. The H–O_H bond length of doped pyrophyllite was longer than that of undoped pyrophyllite. In addition, the average Al_2–O_H bond length of doped pyrophyllite was longer than that of undoped pyrophyllite, whereas the Al_2–O_a bond length of doped pyrophyllite was shorter than that of undoped pyrophyllite (Putra *et al.*, 2019). The average Si_2–O_a

Table 3. The calculated average bond lengths of the undoped and doped pyrophyllites.

Phase	Undoped	Na-doped	K-doped	Mg-doped	Ca-doped	Fe-doped
H–O_H	0.970	0.979	0.978	0.975	0.977	0.974
Al_2–O_H	1.894	1.930	1.897	1.919	1.918	1.898
Al_2–O_a	1.929	1.901	1.904	1.916	1.903	1.929
Na–O_H	–	2.237	–	–	–	–
Na–O_a	–	2.216	–	–	–	–
K–O_H	–	–	2.501	–	–	–
K–O_a	–	–	2.544	–	–	–
Mg–O_H	–	–	–	2.052	–	–
Mg–O_a	–	–	–	2.046	–	–
Ca–O_H	–	–	–	–	2.243	–
Ca–O_a	–	–	–	–	2.255	–
Fe–O_H	–	–	–	–	–	1.920
Fe–O_a	–	–	–	–	–	1.966
Si_2–O_a	1.646	1.640	1.635	1.630	1.628	1.650
Si_2–O_b	1.628	1.625	1.629	1.628	1.628	1.624

and Si_2–O_b bond lengths of doped pyrophyllite were shorter than those of undoped pyrophyllite. Finally, the orders of bond lengths of doping atoms with oxygen atoms were K–O_H > Ca–O_H > Na–O_H > Mg–O_H > Fe–O_H > Al_2–O_H and K–O_a > Ca–O_a > Na–O_a > Mg–O_a > Fe–O_a > Al_2–O_a.

As shown in Fig. 1b, the changes of layer thickness before and after doping of pyrophyllite were also calculated (Table 4), where d_I was the thickness of the two-dimensional layer, d_{T1} was the thickness of the tetrahedral (SiO$_4$) sheet, and d_o was the thickness of the octahedral (AlO$_6$) sheet (Qin *et al.*, 2020). Compared with the values of the undoped pyrophyllite, the d_o values of Na(I)-, K(I)-, Mg(II)- and Ca(II)-doped pyrophyllite increased by 0.43%, 6.69%, 0.05% and 2.09%, respectively, whereas the value of Fe(II)-doped pyrophyllite decreased by 1.23%. Moreover, the d_{T1} values of Na(I)-, Mg(I)-, Ca(II)- and Fe(II)-doped pyrophyllite were greater than that of the undoped pyrophyllite by 0.32%, 1.75%, 0.32% and 1.30%, respectively, whereas the d_{T1} value of K(I)-doped pyrophyllite was less than that of undoped pyrophyllite by 0.69%. Finally, the interlayer thickness d_I of the doped pyrophyllite was reduced compared with that of the undoped pyrophyllite. All of the above results demonstrate that doping has an influence on the lattice parameters, interlayer thickness and bond lengths of pyrophyllite.

Effects on the electronic properties of pyrophyllite

The PDOS, TDOS and band structure of the undoped and doped pyrophyllites were calculated to determine the effects of defects on the electronic properties of pyrophyllite in detail (Tunega *et al.*, 2012).

Figure 2 presents the band structure of pyrophyllite along the high-symmetry lines of the Brillouin zone (BZ). G(0, 0, 0), F(0,

Table 2. The lattice parameters of the undoped and doped pyrophyllites.

Parameter	Experimental data (Lee *et al.*, 1981)	Undoped	Na-doped	K-doped	Mg-doped	Ca-doped	Fe-doped
a (Å)	5.160	5.171	5.184	5.159	5.180	5.189	5.170
b (Å)	8.966	8.978	9.057	9.121	9.012	9.091	8.987
c (Å)	9.347	9.326	9.225	9.198	9.276	9.185	9.318
α	91.18	90.79°	90.91°	89.75°	90.94°	90.73°	90.96°
β	100.46	100.77°	100.89°	100.71°	100.82°	101.03°	100.76°
γ	89.64	89.86°	89.98°	90.68°	89.89°	90.06°	89.79°

Table 4. The average layer thicknesses and interlayer thicknesses of the undoped and doped pyrophyllites.

| Phase	Undoped	Na-doped	K-doped	Mg-doped	Ca-doped	Fe-doped
d_o (Å)	2.107	2.116	2.248	2.108	2.151	2.081
d_{T1} (Å)	2.169	2.176	2.154	2.207	2.176	2.200
d_I (Å)	2.704	2.560	2.565	2.599	2.548	2.668

0.5, 0), Q(0, 0.5, 0.5) and Z(0, 0, 0.5) were the high-symmetry BZ points of pyrophyllite (Zhao *et al.*, 2021b; Wang *et al.*, 2022). The electronic energy band structure of the undoped pyrophyllite was 5.54 eV, as shown in Fig. 2a. The Z point was the valence band maximum (VBM) of the undoped pyrophyllite, while the G point was the conduction band minimum (CBM). Figure 2b–f shows the band structure of Na(I)-, K(I)-, Mg(II)-, Ca(II)- and Fe(II)-doped pyrophyllite, with gap widths of 5.65, 5.33, 5.59, 5.54 and 2.04 eV, respectively. The VBMs of Na(I)-, K(I)-, Mg (II)-, Ca(II)- and Fe(II)-doped pyrophyllite were the Q, G, Q, Z and Q points, respectively, while the CBMs of all of the doped pyrophyllite band structures were at the G point. These results show that the effects of Fe(II) doping on band structure of pyrophyllite were the greatest, while the least effects were observed for Ca(II) doping of pyrophyllite. All of the undoped and doped pyrophyllites remained as insulators, which is one of the reasons why pyrophyllite can be used as a pressure transmission medium and in dielectric ceramics and other fields.

The PDOS and TDOS of undoped and doped pyrophyllites are depicted in Fig. 3a–f. The Fermi energy level was set as the reference point and assigned a value of 0. The PDOSs of O1, O2 and O3 were plotted in Fig. 3 separately because these three kinds of oxygen atoms have different symmetries and positions in the unit cell. The PDOSs of these three atoms were similar to each other. A large charge transfer to the O 2p states from the Al 3p, Na 2p, K

3p, Mg 2p, Ca 3p and Fe 3d states occurred because of the high electronegativity of oxygen. This phenomenon led to the observed similarity. As shown in Fig. 3a, in the wide energy range of 10 eV < E < E$_F$, the valence bands primarily consisted of O 2p states. Furthermore, some residual charges were also to be found in the Al 3s/3p and Si 3s/3p states. The covalent components of the Al–O and Si–O chemical bonds of pyrophyllite were observed. Compared with the PDOS of Al atoms, Mg(II) doping of pyrophyllite led to similar valence bands in the energy range 10 eV < E < E$_F$, composed of O 2p states. Doping of Na 2p, K 3p and Ca 3p states transferred fewer electrons to O 2p states than Al 3p states. After Fe(II) doping of pyrophyllite, the PDOS of the O atoms changed significantly, and strong hybridization between the O p and Fe d orbitals occurred because the O atoms presented new peaks and aligned with the bonding orbital of Fe(II). This phenomenon was due to the charge redistribution resulting from the varying electronegativities of the doping elements and O atoms. This redistribution led to a global electrostatic attraction between the O atoms and Na(I), K(I), Mg(II), Ca(II) and Fe(II) after doping of pyrophyllite (Zhao & He, 2014).

Effects on the mechanical properties of pyrophyllite

As is well known, the mechanical properties of a material are crucial in engineering, industry and other applications. Elastic properties represent the innate properties of a material (Zhao & He, 2014) that indicate the degree to which it can deform under external stress (Pawley *et al.*, 2002). The mechanical properties of undoped and doped pyrophyllites were investigated systematically. The elastic stiffness constants (C_{ij}) of a crystalline system are essential parameters that describe the mechanical properties of its materials, such as its bulk modulus, Young's modulus, *etc.* (Yang *et al.*, 2018). Pyrophyllite is a triclinic system with 21 independent elastic stiffness constants (Benazzouz & Zaoui, 2012).
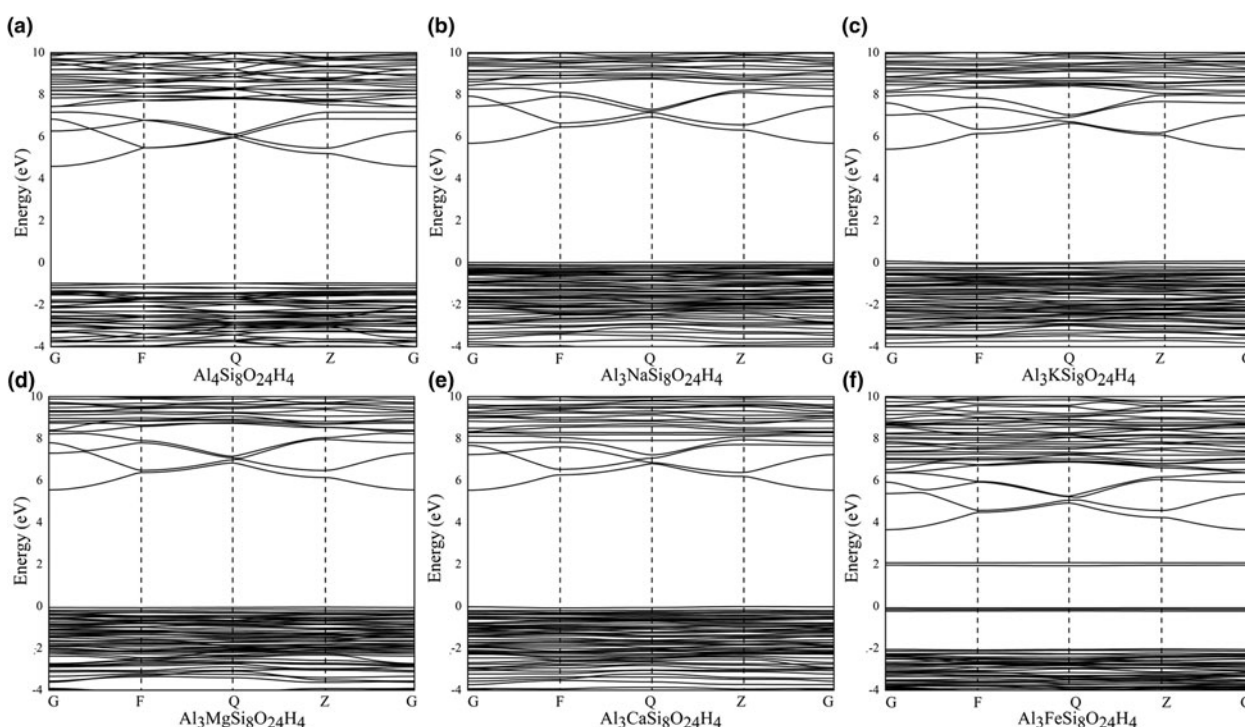
Figure 2. The band structures of the (a) undoped, (b) Na-doped, (c) K-doped, (d) Mg-doped, (e) Ca-doped and (f) Fe-doped pyrophyllites.
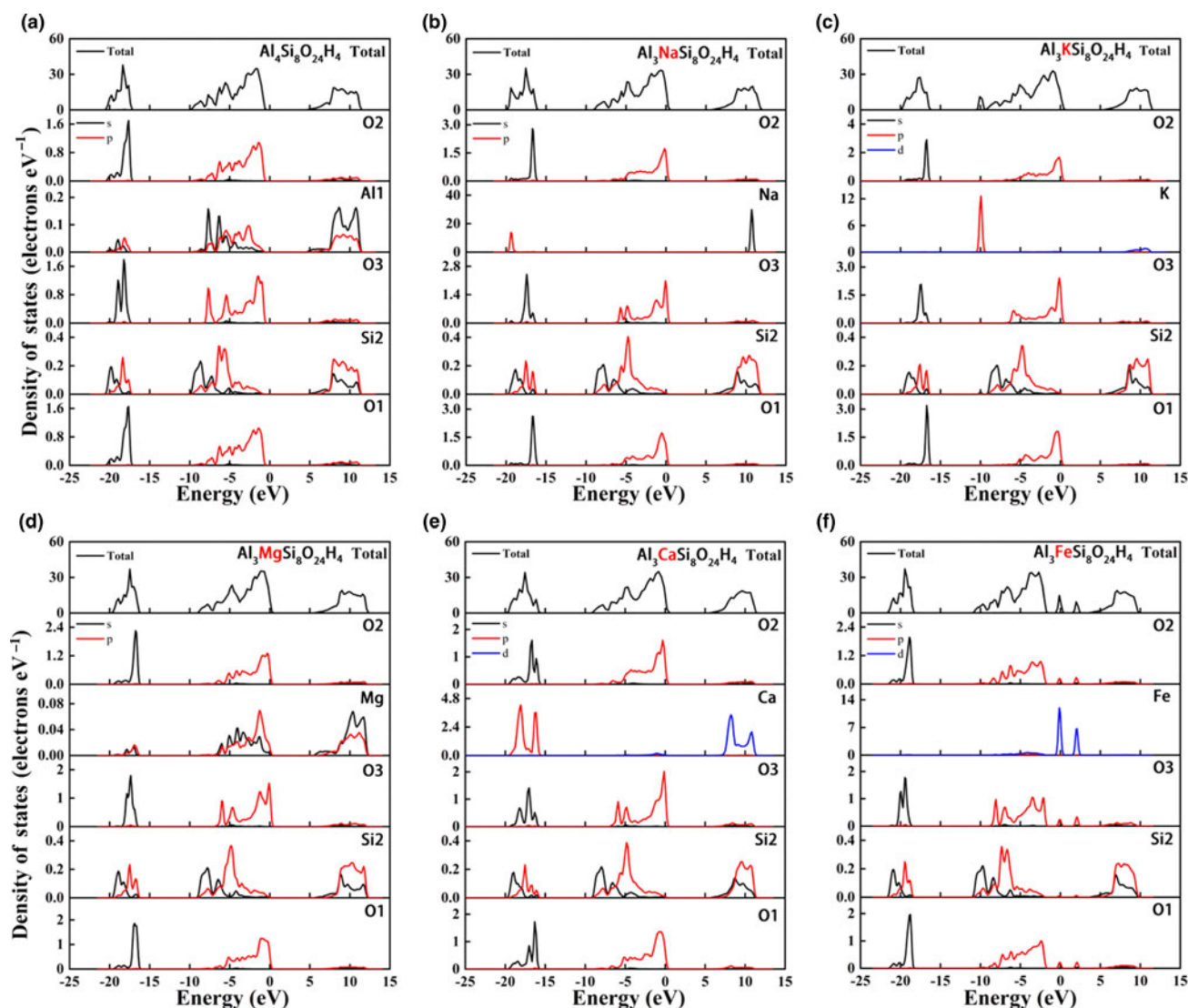
Figure 3. The total and partial densities of states of the (a) undoped, (b) Na-doped, (c) K-doped, (d) Mg-doped, (e) Ca-doped and (f) Fe-doped pyrophyllites.

C_{11}, C_{22}, C_{33}, C_{44}, C_{55}, C_{66}, C_{12}, C_{13}, C_{14}, C_{15}, C_{16}, C_{23}, C_{24}, C_{25}, C_{26}, C_{34}, C_{35}, C_{36}, C_{45}, C_{46} and C_{56} were calculated (Zhao *et al.*, 2020). The results for the undoped and doped pyrophyllites are listed in Table 4. First, the results of the present first-principles calculation for the undoped pyrophyllite were similar to previous experimental data (Cheng *et al.*, 2013) and other previously calculated results (Zartman *et al.*, 2010; Li, 2016), meaning that the present computational approach is highly reliable. Furthermore, it was found that the Born–Huang criteria (Huang *et al.*, 2019) were satisfied for all C_{ij} of the undoped and doped pyrophyllites, indicating that the triclinic undoped and doped pyrophyllites were mechanically stable.

Finally, the calculated longitudinal classic constants of the undoped pyrophyllite were C_{11} = 183.19 GPa, C_{22} = 196.92 GPa and C_{33} = 51.58 GPa, as shown in Table 4. The elastic constant C_{11} was less than C_{22}, indicating that the anti-deformation ability of the *b*-axis was stronger than that of the *a*-axis. Consistent with expectations, the crystal exhibited the greatest susceptibility to deformation along the *c*-axis, as represented by the elastic constant C_{33}. In addition, the elastic constant C_{66} was greater than C_{44} and C_{55}, indicating that the shear deformation resistances

of the (100) and (010) planes were weaker than that of the (001) plane. It was found that C_{11}, C_{22}, C_{33} and C_{66} of doped pyrophyllite were less than those of undoped pyrophyllite. In particular, C_{11} of the K(I)-doped pyrophyllite decreased the most (by 28.02%), C_{22} of the K(I)-doped pyrophyllite decreased the most (by 31.64%), C_{33} of the Na(I)-doped pyrophyllite decreased the most (by 20.32%) and C_{66} of the K(I)-doped pyrophyllite decreased the most (by 25.72%). However, C_{44} of Na(I), Mg(II), Ca(II) and Fe(II)-doped pyrophyllite were greater than those of undoped pyrophyllite, and C_{44} of Fe(II)-doped pyrophyllite was less than that of undoped pyrophyllite. In addition, C_{55} of Mg(II)-, Na(I)- and Ca(II)-doped pyrophyllite increased and C_{55} of K(I)- and Fe(II)-doped pyrophyllite decreased. The other elastic constants of the doped pyrophyllite demonstrated clear changes. The above results for all of the doped pyrophyllites indicated that the anti-deformation abilities of the *a*-axis and *b*-axis were stronger than that of the *c*-axis, and the deformation ability of the three axes of the undoped pyrophyllite was stronger than that of doped pyrophyllite. The shear deformation resistance of the (001) plane of the doped pyrophyllite was stronger than those of the (100) and (010) planes and weaker than that of the

Table 5. The calculated elastic constants of the undoped and doped pyrophyllites.

Elastic constant	Undoped		Na-doped	K-doped	Mg-doped	Ca- doped	Fe-doped
	Previous calculation (Li *et al.*, 2016)	Calculated					
C_{11}	189.62	183.19	146.20	131.87	163.56	176.89	173.34
C_{22}	181.63	196.92	173.91	134.62	168.03	192.58	178.12
C_{33}	67.12	51.58	41.10	48.95	51.29	42.83	49.54
C_{44}	22.13	22.51	35.52	25.23	26.44	29.28	21.83
C_{55}	12.00	19.63	25.25	19.38	22.34	22.63	19.34
C_{66}	79.10	77.54	58.85	57.60	68.84	66.11	74.62
C_{12}	42.73	40.85	50.65	72.31	58.27	70.68	57.47
C_{13}	5.05	21.34	38.55	4.02	32.93	24.79	21.39
C_{14}	–	1.01	−9.06	−0.65	−2.42	−9.79	1.58
C_{15}	–	−31.98	−28.64	−24.04	−30.30	−35.18	−29.36
C_{16}	–	−10.55	−5.34	−0.79	−9.64	−12.12	−9.18
C_{23}	6.29	12.48	19.17	18.37	29.53	18.50	10.90
C_{24}	–	−2.92	−16.13	7.71	1.14	−11.95	0.13
C_{25}	–	−11.46	−17.79	−22.74	−10.03	−16.16	−8.14
C_{26}	–	−3.08	0.61	−4.93	3.68	−0.89	0.92
C_{34}	–	−19.45	−20.44	−19.67	−21.96	−3.18	−15.38
C_{35}	–	0.16	−0.90	6.46	−2.20	−12.62	18.33
C_{36}	–	0.36	11.90	11.94	−9.98	8.02	2.18
C_{45}	–	−4.53	−9.69	−9.79	−8.06	−10.80	−7.25
C_{46}	–	−12.82	−14.13	−6.40	−11.92	−14.77	−12.04
C_{56}	–	0.12	1.48	−5.47	−0.65	−6.56	0.21

undoped pyrophyllite. The above results show that the effects of doping on the mechanical properties of pyrophyllite were significant.

The VRH approach (Hill, 1952; Chung & Buessem, 1968) is a suitable method for calculating the *B*, *G* and *Y* of pyrophyllite. These parameters are crucial indicators of the mechanical behaviour of materials, and they play a significant role in characterizing their overall mechanical properties. The elastic parameters of the undoped and doped pyrophyllites are listed in Table 5. The *B* value of undoped pyrophyllite was 45.94 GPa, while the *B* values of Na(I)-, K(I)-, Mg(II)-, Ca(II)- and Fe(II)-doped pyrophyllite were 40.93, 39.12, 44.66, 43.71 and 43.67 GPa, respectively. These results indicate that the resistance to volume change due to strain stress and fracture of doped pyrophyllite was weaker than that of undoped pyrophyllite. The *G* value denotes the tendency of an object to shear when the material is subjected to an opposing force. As listed in Table 6, the *G* values of all of the doped pyrophyllites were smaller than that of undoped pyrophyllite. In particular, the *G* value of K(I)-doped pyrophyllite decreased the most. The stiffness of a material can be illustrated by Young's modulus (*Y*). Compared with the *Y* value of the undoped pyrophyllite, the *Y* values of the Na(I)-, K(I)-, Mg(II)-,

Ca(II)- and Fe(II)-doped pyrophyllite decreased by 15.27%, 24.49%, 16.35%, 19.48% and 18.78%, respectively. These results demonstrate that the doping reduced the ability of pyrophyllite to resist external pressure and shear strain and reduced its rigidity, indicating that the pyrophyllite was easier to deform under external force after doping.

The Poisson's ratio μ serves as an indicator of the bonding nature of materials (Yang *et al.*, 2018). The calculated μ value for the undoped pyrophyllite, as listed in Table 6, was found to be 0.20. This value suggests a strong covalent characteristic in the chemical bonding of pyrophyllite. Furthermore, as μ was less than the critical value of 0.27, this indicates that the material can be expected to be brittle. In terms of the effects of doping on pyrophyllite, the μ values of the Na(I)-, K(I)-, Mg(II)-, Ca(II)- and Fe(II)-doped pyrophyllite increased to 0.22, 0.24, 0.24, 0.25 and 0.25, respectively. These results also indicate the strong covalent aspect to the chemical bonds of pyrophyllite after doping.

In addition, the empirical *G/B* ratio (Pugh, 2009; Fan *et al.*, 2015) can serve as an indicator of the brittle or ductile behaviour of materials. When the *G/B* ratio is <0.57, this suggests a material will demonstrate ductile behaviour. Conversely, if the *G/B* ratio is >0.57, the material can be expected to exhibit brittle behaviour

Table 6. The calculated elastic mechanical parameters of the undoped and doped pyrophyllites.

Phase	Undoped		Na-doped	K-doped	Mg-doped	Ca- doped	Fe-doped
	Experimental data (Cheng *et al.*, 2013)	Calculated					
B (GPa)	14.8–37.5	45.94	40.93	39.12	44.66	43.71	43.67
Y (GPa)	38.6–53.6	82.00	69.47	61.91	68.59	66.02	66.60
G (GPa)	18.2–21.3	34.09	28.54	25.04	27.56	26.45	26.73
μ	0.06–0.26	0.20	0.22	0.24	0.24	0.25	0.25
G/B	–	0.74	0.69	0.64	0.62	0.61	0.61
*H*v (GPa)	–	8.05	6.27	4.77	4.88	4.51	4.66
V_p (km s^{-1})	3.78–4.91	6.30	5.84	5.04	5.40	5.25	5.21
V_s (km s^{-1})	2.58–2.79	3.85	3.51	2.96	3.15	3.04	3.02

(Yang *et al.*, 2018). The *G/B* ratios of the undoped and doped pyrophyllites were greater than the critical value of 0.57, so they also showed brittle behaviour.

The v_p and v_s values are also listed in Table 6, and these are key quantities in the interpretation of seismic data. Compared with the undoped pyrophyllite, the obtained v_p and v_s values of the doped pyrophyllite were lower. In particular, the v_p and v_s values of K(I)-doped pyrophyllite decreased the most, demonstrating values of 5.04 and 2.96 km s^{-1}, respectively. After doping, the Vickers hardness of pyrophyllite decreased, so the pyrophyllite gained a soapy and smooth surface, suggesting that doped pyrophyllite could be used in the pharmaceutical industry.

The degree of dependence of the modulus of elasticity of pyrophyllite in all directions can be determined from anisotropy data. Ranganathan & Ostoja-Starzewski (2008) proposed an index of universal anisotropy that is applicable to all crystalline forms to assess differences in anisotropy, and this index is denoted by the symbol A^U. The A^U index is based on the upper and lower bounds of the bulk and shear moduli, and A^U can be defined as per Equation 8:

$$A^U = 5\frac{G_V}{G_R} + \frac{B_V}{B_R} - 6 \tag{8}$$

The degree of deviation of the A^U value from 0 reflects the degree of anisotropy of the material. To determine the anisotropy of pyrophyllite before and after doping, three-dimensional diagrams of the Young's modulus (Roman *et al.*, 2016) of undoped and Na(I)-, K(I)-, Mg(II)-, Ca(II)- and Fe(II)-doped pyrophyllite were drawn, as shown in Fig. 4a–f. The three-dimensional diagrams of the Young's modulus were close to spherical, and the degree of irregularity of the sphere represented the degree of anisotropy of the material. In addition, the anisotropies of undoped and Na(I)-, K(I)-, Mg(II)-, Ca(II)- and Fe(II)-doped pyrophyllite were calculated to be 8.04, 10.14, 8.31, 11.61, 14.95 and 12.72, respectively. These results indicate that both undoped and doped pyrophyllites showed anisotropy (Zhao & Xu, 2000), with the degree of anisotropy becomes greater after doping.

Conclusion

In this work, the effects of Na(I), K(I), Mg(II), Ca(II) and Fe(II) doping on the atomic structure, electronic properties and mechanical characteristics of pyrophyllite were determined using the DFT. The following conclusions can be drawn from the research:

(1) Compared to the atomic structure of the undoped pyrophyllite, the structures of the Na(I)-, K(I)-, Mg(II)-, Ca(II)- and Fe(II)-doped pyrophyllites changed significantly. The influence of K(I) doping on the lattice parameters of pyrophyllite was the greatest, while the least influence was observed for Fe(II) doping. After doping, the orders of bond lengths of doping atoms with oxygen atoms were K–O_H > Ca–O_H > Na–O_H > Mg–O_H > Fe–O_H > Al$_2$–O_H and K–O_a > Ca–O_a > Na–O_a > Mg–O_a > Fe–O_a > Al$_2$–O_a. After doping, the layer thicknesses of Na(I)-, K(I)-, Mg(II)-, Ca(II)- and Fe(II)-doped pyrophyllites were reduced compared with that of the undoped pyrophyllite.

(2) In addition, the PDOSs, TDOSs and energy band structures of the five kinds of doped pyrophyllite also changed significantly. The order of impact on the band structure of pyrophyllite was Fe(II) > K(II) > Na(I) > Mg(I) > Ca(II). These features were caused by the differing electronegativities of the doping atoms and the oxygen atoms.

(3) Finally, the elastic constants of the doped pyrophyllites were lower than that of the undoped pyrophyllite. The deformation ability of the three axes of the doped pyrophyllites and the shear deformation resistance in the (001) plane of the doped pyrophyllites were weaker than those of the undoped pyrophyllite. Doping reduced the *B*, *G*, *Y*, v_p and v_s values but increased the A^U value of pyrophyllite. The order of impact on the mechanical properties of pyrophyllite was Mg(II) > Fe(II) > Ca(II) > K(I) > Na(I).

The first-principles results obtained in the present work provide valuable insights in the physicochemical and mechanical properties of the substitutional defects in pyrophyllite at the molecular level.
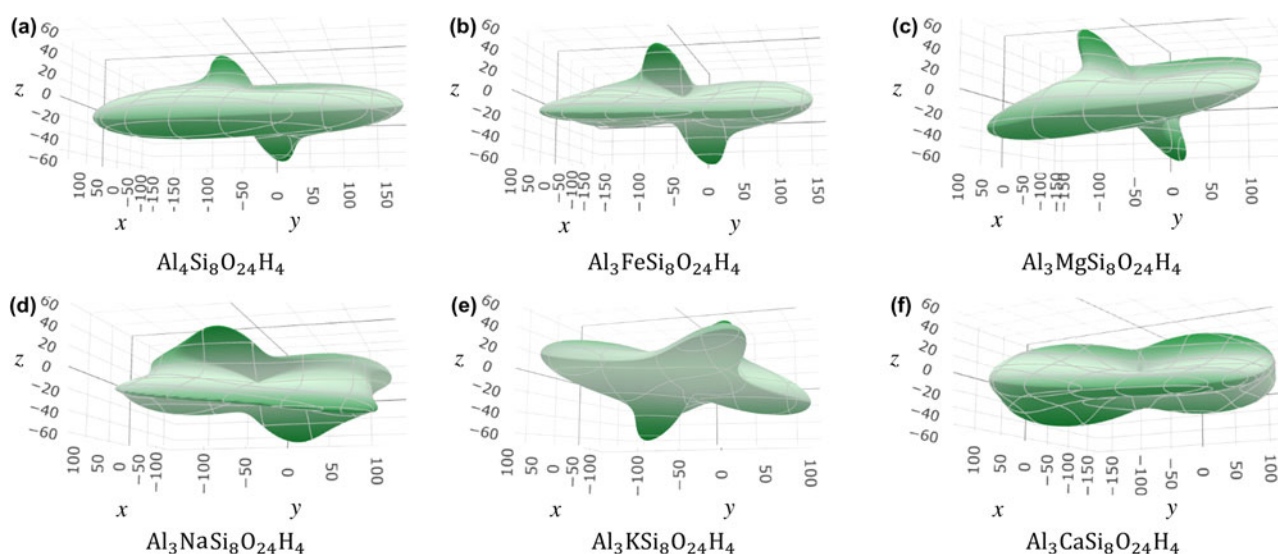

Figure 4. There-dimensional diagrams of the Young's modulus of the (a) undoped, (b) Na-doped, (c) K-doped, (d) Mg-doped, (e) Ca-doped and (f) Fe-doped pyrophyllites.

Competing interests. The authors declare none.

Data availability. The raw/processed data required to reproduce these findings cannot be shared at this time due to technical or time limitations. Requests for data 6 months after publication of this article will be considered by the corresponding author.

References

Ali M.A., Ahmed H.A.M., Ahmed H.M. & Hefni M. (2021) Pyrophyllite: an economic mineral for different industrial applications. *Applied Sciences*, **11**, 11357.

Benazzouz B.K. & Zaoui A. (2012) Phase diagram of kaolinite from molecular dynamics calculations. *Physica B: Condensed Matter*, **407**, 2462–2470.

Bentayeb A., Amouric M., Olives J., Dekayir A. & Nadiri A. (2003) XRD and HRTEM characterization of pyrophyllite from Morocco and its possible applications. *Applied Clay Science*, **22**, 211–221.

Bruno M., Prencipe M. & Valdre' G. (2006) *Ab initio* quantum-mechanical modeling of pyrophyllite [$Al_2Si_4O_{10}(OH)_2$] and talc [$Mg_3Si_4O_{10}(OH)_2$] surfaces. *Physics and Chemistry of Minerals*, **33**, 63–71.

Chen J., Xie X.Y., Zhang S.B. & Sun Y.Y. (2020) Benchmarking PBE+D3 and SCAN+rVV10 methods using potential energy surfaces generated with MP2+Delta CCSD(T) calculation. *Chinese Physics B*, **29**, 251–256.

Cheng Q.L., Sondergeld C. & Rai C. (2013) Experimental study of rock strength anisotropy and elastic modulus anisotropy. *Seg Technical Program Expanded Abstracts*, **2013**, 362–367.

Chung D.H. & Buessem W.R. (1968) The Voigt–Reuss–Hill (VRH) approximation and the elastic moduli of polycrystalline ZnO, TiO_2 (rutile), and α-Al_2O_3. *Journal of Applied Physics*, **39**, 2777–2782.

Du P.X. & Yuan P. (2019) Studies and application of pyrophyllite in key minerals material areas such as superhard materials. *Conservation and Utilization of Mineral Resources*, **39**, 87–92.

Fan Q.Y., Wei Q., Chai C.C., Yu X.H., Liu Y., Zhou P.K. *et al.* (2015) First-principles study of structural, elastic, anisotropic, and thermodynamic properties of R3-B2C. *Chinese Journal of Physics*, **53**, 100601.

Gruner J.W. (1934) The crystal structures of talc and pyrophyllite. *Zeitscbrift Kristallographica*, **55**, 412419.

Hill R. (1952) The elastic behavior of a crystalline aggregate. *Proceedings of the Physical Society (Section A)*, **65**, 349.

Hou J.L., Chen M., Zhou Y.F., Bian L., Dong F.Q., Tang Y.H. *et al.* (2020) Regulating the effect of element doping on the CO_2 capture performance of kaolinite: a density functional theory study. *Applied Surface Science*, **512**, 145642.

Huang H.M., Jiang Z.Y., Yang J.T., Xiong Y.C., He Z.D. & Zhu Z.W. (2019) First principles study of RbVF3: a spin gapless semiconductor under high pressure. *Chinese Journal of Physics*, **25**, 132–136.

Katti D.R., Schmidt S.R., Ghosh P. & Katti K.S. (2005) Modeling the response of pyrophyllite interlayer to applied stress using steered molecular dynamics. *Clays and Clay Minerals*, **53**, 171–178.

Kremleva A., Martorell B., Kruger S. & Rosch N. (2012) Uranyl adsorption on solvated edge surfaces of pyrophyllite: a DFT model study. *Physical Chemistry Chemical Physics*, **14**, 5815–5823.

Kresse A.G. & Furthmüller B.J. (1996) Efficiency of *ab-initio* total energy calculations for metals and semiconductors using a plane-wave basis set. *Computational Materials Science*, **6**, 15–50.

Lavikainen L.P., Hirvi J.T., Kasa S., Schatz T. & Pakkanen T.A. (2015) Stability of dioctahedral 2:1 phyllosilicate edge structures based on pyrophyllite models. *Theoretical Chemistry Accounts*, **134**, 112.

Lee J.H. & Guggenheim S. (1981) Single-crystal X-ray refinement of pyrophyllite-1Tc. *American Mineralogist*, **66**, 350–357.

Li H.T. (2016) *First-Principles Study on Microstructures and Elastic Properties of Clay Minerals* PhD thesis. Taiyuan University of Technology, Taiyuan, China.

Luna C.R., Reimers W.G., Avena M.J. & Juan A. (2021) Theoretical study of the octahedral substitution effect in delaminated pyrophyllite: physicochemical

properties and applications. *Physical Chemistry Chemical Physics*, **23**, 14601–14607.

Pawley A., Clark S. & Chinnery N. (2002) Equation of state measurements of chlorite, pyrophyllite, and talc. *American Mineralogist*, **87**, 1172–1182.

Perdew J.P., Burke K. & Ernzerhof M. (1996) Generalized gradient approximation made simple. *Physical Review Letters*, **77**, 3865–3868.

Pugh S.F. (2009) Relations between the elastic moduli and the plastic properties of polycrystalline pure metals. *Philosophical Magazine*, **45**, 823–843.

Putra S.E.M., Muttaqien F., Hamamoto Y., Inagaki K. & Morikawa Y. (2019) Van der Waals density functional study of formic acid adsorption and decomposition on Cu(111). *Journal of Chemical Physics*, **150**, 154707.

Qin X.Z., Zhao J., Wang J.M. & He M.C. (2020) Atomic structure, electronic, and mechanical properties of pyrophyllite under pressure: a first-principles study. *Minerals*, **10**, 778.

Ranganathan S.I. & Ostoja-Starzewski M. (2008) University elastic anisotropy index. *Physical Review Letters*, **101**, 055504.

Reddy T.R., Reddy S.L. & Endo T. (2016) Structural characterization studies on the natural mineral pyrophyllite. *Radiation Effects and Defects in Solids*, **171**, 307–315.

Refson K., Park S.H. & Sposito G. (2003) *Ab initio* computational crystallography of 2:1 clay minerals: 1. pyrophyllite-1Tc. *Journal of Physical Chemistry B*, **107**, 13376–13383.

Roman G., Pullumbi P. & Coudert F.X. (2016) *ELATE*: an open-source online application for analysis and visualization of elastic tensors. *Journal of Physics: Condensed Matter*, **28**, 275201.

Shi B., Liu X., Xin M.M., Lin Y.H., Zhao Y.P. & Liu Q.F. (2017) Mineralogic characteristics of pyrophyllite mudstone in Mentougou, western Beijing. *Goal Geology & Exploration*, **45**, 25–31.

Tunega D., Bŭcko T. & Zaoui A. (2012) Assessment of ten DFT methods in predicting structures of sheet silicates: importance of dispersion corrections. *Journal of Chemical Physics*, **137**, 114105.

Walle G.G.V. & Neugebauer J. (2004) First-principles calculations for defects and impurities: applications to III-nitride. *Journal of Applied Physics*, **95**, 3851–3897.

Wang J.M., Zhao J., Qiao Y.F. & Luan Z.L. (2022) Effect of Mg(II), Mn(II), and Fe(II) doping on the mechanical properties and electronic structure of calcite. *Materials Today Communications*, **31**, 103725.

Yan J., Zhang J., Fang W., Dong N., Shao J.M. & Sheng J.W. (2013) Microstructural alteration of pyrophyllite by dry grinding. *Journal of Chemical Engineering of Chinese Universities*, **27**, 344–347.

Yang Y., Wang W., Gan G.Y., Shi X.F. & Tang B.Y. (2018) Structural, mechanical and electronic properties of (TaNbHfTiZr)C high entropy carbide under pressure: *ab initio* investigation. *Physica B – Condensed Matter*, **550**, 163–170.

Zartman G.D., Liu H., Akdim B., Pachter R. & Heinz H. (2010) Nanoscale tensile, shear, and failure properties of layered silicates as a function of cation density and stress. *Journal of Physical Chemistry C*, **114**, 1763–1772.

Zhang G.P., Wei Z.X., Ferrell R.E., Guggenheim S., Cygan R.T. & Luo J. (2010) Evaluation of the elasticity normal to the basal plane of non-expandable 2:1 phyllosilicate minerals by nanoindentation. *American Mineralogist*, **95**, 863–869.

Zhang L.L., Lin, F., Lv Z., Xiao L.Y., He X.L., Wang W.L. & Li L.W. (2014) Research and development of pyrophyllite and its current application status in China. *Superhard Material Engineering*, **26**, 35–38.

Zhao J. (2013) *The Research on Defect Formation Mechanism and Adsorption Property of Clay Minerals in Soft Rock*. PhD thesis. Chinese University of Mining and Technology, Beijing, China.

Zhao J. & He M.C. (2014) Theoretical study of heavy metal Cd, Cu, Hg, and Ni(II) adsorption on the kaolinite(001) surface. *Applied Surface Science*, **317**, 718–723.

Zhao M.J. & Xu R. (2000) Research status and prospect of rock acoustic properties. *Journal of Chongqing Jiaotong Institute*, **19**, 79–85.

Zhao J., Qin X.Z., Wang J.M. & He M.C. (2020) Effect of Mg(II) and Na(I) doping on the electronic structure and mechanical properties of kaolinite. *Minerals*, **10**, 368.

Zhao J., Cao Y., Wang L. & Zhang H.J. (2021a) Investigation on atomic structure and mechanical property of Na- and Mg-montmorillonite under high pressure by first-principles calculations. *Minerals*, **11**, 613.

Zhao J., Wang Z., Gao W., Wang Y.F. & Huang B.W. (2021b) Theoretical investigation on rare earth elements of Y, Nd and La atoms' adsorption on the kaolinite (001) and (00$\bar{1}$) surfaces. *Minerals*, **11**, 856.